# Microwave-Reduced Uncapped Metal Nanoparticles on Graphene: Tuning Catalytic, Electrical, and Raman Properties

Kabeer Jasuja, Josh Linn, Steven Melton, and Vikas Berry*

1011 Durland Hall, Department of Chemical Engineering, Kansas State University, Manhattan, Kansas 66502

ABSTRACT This work addresses a major challenge in liquid-phase catalysis by enabling the synthesis of solvent dispersible "uncapped" metal nanoparticles (NPs) with enhanced density of accessible catalytic sites. We demonstrate that graphene oxide's (GO's) high density of accessible and bondable oxy-functional groups and the high steric hindrance from its micrometer-scale area covalently implant, stabilize, and support bare-surfaced gold nanoparticles (BSGNs) produced in situ by a unique microwave reduction process. Comparing the efficiency of catalytic reduction of p-nitroaniline (p-NA) by BSGNs and similar sized surfactant-capped gold NPs showed that the uncapped surface on GO-supported NPs, (a) opens up 258 % more active sites, and (b) enhances the catalytic reduction of p-NA by 10−100 fold. Further, BSGN implantation on GO, (a) amplifies the Raman signal of bare GO by ∼3 fold, and (b) increases the conductivity of native p-type GO by > 10 fold via injection of 1.328×10^{12} electrons/cm^2, consequently transforming it into an n-type semiconductor.

SECTION Nanoparticles and Nanostructures

GO sheet decorated with BSGNs
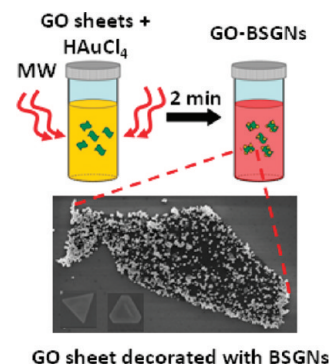
Recently, single-atom thick, quasi-planar graphene sheets with sp^2 bound carbon atoms arranged in a honeycomb lattice have generated tremendous research interest owing to their fascinating electronic,[1−3] optical,[4−6] and mechanical[7] properties. Functionalized graphene sheets with arguably the largest surface area per volume, high density of interfacable chemical groups, and preserved semiconducting properties at room temperature are being leveraged for unique applications such as biosensing,[8−10] chemical sensing,[11] field emission,[12] membrane fabrication,[13] and nanocomposite fabrication.[14,15] These systems were realized by converting a fraction of the sp^2 graphenic carbons to oxygenated sp^3 carbons, which covalently bind with polymers,[14,15] chemicals,[16,17] biomolecules,[8−10] and micro/nanostructures.[18−21] Of these, graphene−nanoparticle composites are gaining great attention owing to the resultant multifunctional and unified properties.[18−20] For example, GO−TiO$_2$ sheets can transfer electrons from a photoexcited TiO$_2$ nanoparticle to another site on GO for catalysis; graphene−palladium nanoparticle sheets can selectively detect hydrogen; graphene−platinum, graphene−palladium, and graphene−platinum−ruthenium nanocomposites exhibit enhanced catalytic activities; and gold nanostructures grown on GO can control its electrical properties and enhance its Raman scattering signal (our earlier work).[19]

Catalytic activity directly scales with the available active sites. Recently, surface-capped gold nanoparticle (GNP) deposition on graphene sheets has been an important research topic;[18,19,21] however, the active sites on GNPs (solution phase) have so far been blocked by the stabilizing molecules.[22,23] Here,

we demonstrate that the local dielectric heating from microwave (MW) exposure of a metal salt solution results in nucleation of reactive naked NPs, which instantaneously implant on the GO sheets in a single step. The oxy-functional groups (carboxylic, epoxy, carbonyl, phenol, lactone, quinone, and hydroxyl groups) on GO chemically bond and stabilize these metal nuclei, thus eliminating the need to cap the catalytically active sites on GNPs. Since one face of the GNPs implant on the GO, the other exposed face is naked with the bare atomic sites. The present study illustrates and characterizes, for the first time, catalytic properties of solvent-dispersed bare-surfaced gold nanoparticles (BSGNs) and compares their efficiency with similar shaped surfactant-capped gold nanoparticles. We also show the structural, Raman, and electrical characterization of BSGNs implanted on GO. The key results demonstrated are that, (a) the structure of BSGNs on GO can be controlled by microwave exposure, (b) BSGNs exhibit 10−100-fold enhancement in catalytic reduction of p-nitroaniline as compared to that of surface-capped or non-naked GNPs with an increase in the effective catalytic site density by 258 %, (c) BSGNs amplify the Raman signal of GO by ∼3 fold, and (d) BSGNs inject ∼1.328×10^{12} electrons/cm^2 in GO, consequently transforming it to an n-type semiconductor. We also demonstrate that GO can be applied to produce bare-surfaced monodisperse GNPs without microwave exposure.
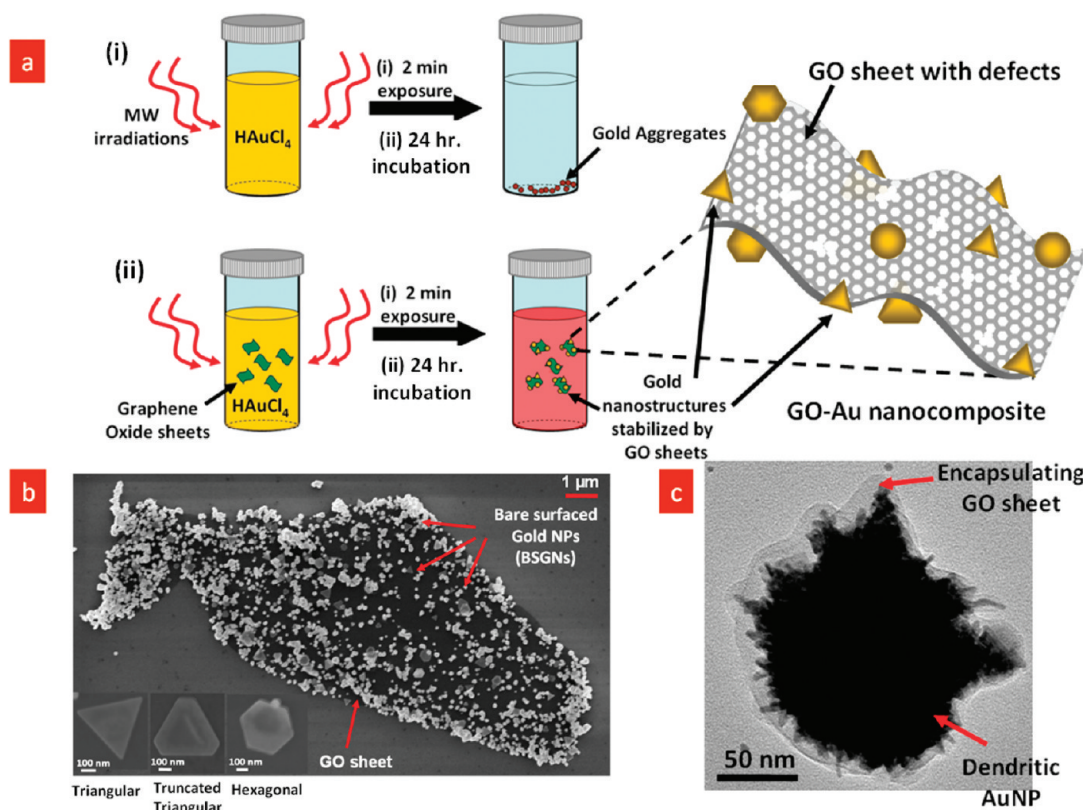
Figure 1. Microwave (MW)-assisted in situ synthesis of multiple shaped bare-surfaced gold nanoparticles (BSGNs) on graphene oxide (GO). (a) An aqueous solution of gold salt, when microwaved for ~2 min, results in the formation of gold nuclei which agglomerate to form clusters (i). However, when the solution mixture also contains GO, the gold nanostructures get templated on the GO sheets (ii). This is attributed to the oxy-functional groups present on GO sheets, which stabilize the Au nuclei. (b) FESEM image of a BSGN-templated GO sheet on a silica substrate. The BSGNs acquire several shapes, such as triangular, truncated-corner triangular, and hexagonal (as shown in the inset). (c) TEM image of a dendritic GNP encapsulated by a GO sheet. These GO-coated NPs are formed via MW exposure on the solution maintained at a lower ambient temperature.

The interaction of the electromagnetic waves with the high dielectric solvent molecules results in a space-confined uniform heating ($E \propto f \varepsilon' (\tan \delta) P^2$, where P is the microwave power, f is the frequency of the microwave, ε' is the dielectric constant of the solvent, and δ is the loss factor). The resultant local temperature rise has been employed to enhance the kinetics of organic reactions[24−26] by utilizing the additional electronic kinetic energy to cross the reaction activation barrier. Similarly, the MW exposure on metal salts significantly reduces the barrier to reduction, nucleation, and ion incorporation, leading to formation of NPs which, due to a higher crystallization rate, have sharper edges than those formed by conventional heating.[27] However, so far, MW-nucleated NPs have been synthesized in the presence of reducing agents and stabilizing molecules such as chitosan, alkyltrimethyl ammonium bromide, and sodium citrate.[27−33] In this study, we have demonstrated that the MW has a self-sufficient ability to induce nucleation of aqueous gold salt even in the absence of chemical reductants, and the nucleated GNPs thus formed can covalently bind (implant) on the GO sheets and become stabilized in solution. This is facilitated by the MW-induced dielectric heating via rapid dipolar rotations of the polarized water molecules that create local high-pressure regions in the salt water system. Near the critical range (150−300 °C), water is known to exhibit a 3-fold higher

dissociation constant, hence functioning both as an acid and a base. We therefore attribute the chemical-free reduction of gold salt to the enhanced dissociation of water caused by local and confined dielectric heating effects from MW.[34] As expected, the GNPs exhibit sharp triangular, truncated triangular, hexagonal, globular, and dendritic morphologies, making them immensely useful for catalytic applications.[35] In the absence of GO, the MW-nucleated GNPs become unstable and aggregate. Therefore, the GO sheets act as swimming substrates on which GNPs imbed and which keep the NPs dispersed (Figure 1a). Further, the stability of the GNPs is unaffected if the GO sheets are added during or immediately after the MW exposure, which indicates that the covalent binding between the GO and GNPs is not MW-actuated . However, when the GO sheets are also present during the MW exposure, they are expected to undergo a partial reduction as prolonged MW exposure (~10 min) has been shown to result in a mild thermal reduction of GO sheets.[36] We also controlled the size distribution of naked GNPs imbedded on GO by a simple, non-MW-based reduction process (shown later). Recently, naked nanoparticles have been implanted on a graphene backbone by substrate-based electrochemical reactions.[11] However, it is challenging to solution-disperse these composites for liquid-phase reactions at high throughput.[21]

The GO–BSGN nanocomposites were synthesized by MW exposure (1.05 kW, 2450 MHz) on an aqueous solution of gold salt, $HAuCl_4 \cdot 3H_2O$ (10 mL, 0.275 mM) and GO (prepared by Hummer's method, 100 μL, 20 mM carboxylic acid quantified by titration) for a time interval between 60 and 300 s with intermittent cooling after every 10 s. The mixture was then allowed to stand for ~24 h, resulting in the formation of anisotropic BSGNs, which assembled on GO sheets (Figure 1). Upon carrying out the MW exposure in a lower ambient temperature (by placing the mixture in an ice bath), we observed the formation of a small incidence of dendritic GNPs, some of which were wrapped with GO sheets, presumably smaller in sizes (Figure 1c). The formation of dendritic nanostructures is explained later.

For structural characterization, the BSGN templated GO sheets were immobilized on an amine-silanized silica surface via electrostatic interfacing (see Supporting Information, Figure S1), which facilitates a selective deposition of only the GO–BSGN sheets separating them from the BSGNs that have not yet interfaced with GO sheets. Figure 1b shows an FESEM image of the immobilized GO–BSGN composite. The majority of the BSGNs exhibit polyhedral shapes with a broad size distribution from 50 to 350 nm, while there is a small fraction of spherical nanoparticles. The broad size and shape distribution is attributed to the absence of growth termination from stabilizing molecules. Later, we show a mechanism to deposit monodisperse bare-surfaced nanoparticles on GO. Since the smaller GNPs are more in number (n) and have a higher surface potential, μ_{GNPs}, and thus higher free energy, they are expected to coagulate and grow to form larger nanoparticles[37] ($\sum_{i=1}^{n}(\mu_{GNPs}N_{GNPs}) > \sum_{i=1}^{m}(\mu_{GNP,L}N_{GNP,L})$, $n > m$, where $\mu_{GNP,L}$ is the surface potential of larger nanoparticles). Since diffusion and nucleation barriers are temperature- and concentration-dependent (explained later), this process could be further controlled by adjusting the MW power and salt concentrations.

BSGNs assemble homogeneously on the GO sheets with a high coverage index, η, of 0.31 ($\eta \equiv$ fraction of GO surface covered by BSGNs), which is attributed to the high density of oxy-functional groups on the surface of GO.[38] Also, the BSGNs are implanted on both sides of the GO sheets. This is evident in the FESEM images of the immobilized BSGN–GO sheets that show a contrast between the BSGNs present on different sides of the GO sheets. The BSGNs on the substrate-facing side of the GO appear darker since they get screened by the GO sheet, while those on the surface of GO sheet directly exposed to the electron beam appear brighter (Figure 3a). The substrate-facing BSGNs also raise and stretch the GO sheets during immobilization, which creates wrinkles (Figure 2, right bottom inset, and Supporting Information, Figure S2).

The absorption spectra of a freshly prepared solution of GO–BSGN composite (Figure 2) exhibits a broad peak centered at ~575 nm, confirming the wide size distribution of gold NPs. Absorption spectra of a nonmicrowaved solution mixture of GO and gold salt kept for > 7 days did not display any significant peak in the visible region nor result in the formation of any gold nanostructures, signifying that GO does not reduce the NPs. This along with the observation that the formation of BSGNs is independent of the order in which the GO sheets are introduced during synthesis (before or after
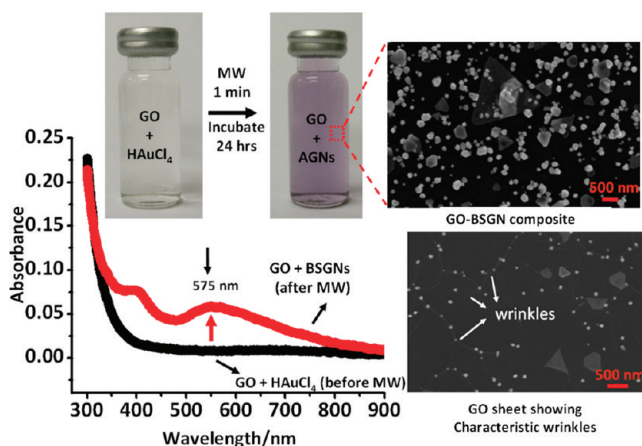

Figure 2. Before the MW exposure, a solution of GO and gold salt does not exhibit a significant peak in the visible region. After the MW exposure, a wide absorption peak centered at ~575 nm appears in the spectrum. The top left inset shows the change in the color of the reactant mixture as it is exposed to MW irradiations. The GNS-decorated GO sheets (top right inset) are immobilized on a Si substrate for FESEM imaging, and the presence of BSGNs results in localized deformation of GO sheets, leading to the formation of wrinkles, the nodes of which are formed by the BSGNs (bottom right inset).
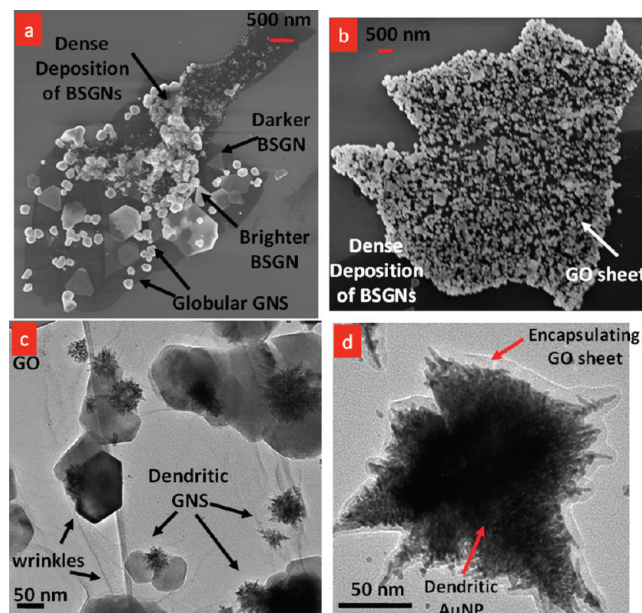

Figure 3. (a) FESEM image of a GO sheet decorated with BSGNs, exhibiting dark and bright contrast. The darker BSGNs are templated on the rear surface of the GO sheet, and the brighter BSGNs are templated on the exposed surface of the GO sheet. (b) FESEM image of a GO sheet that was immobilized ~72 h after being incubated in the microwave gold salt solution, exhibiting a high surface coverage index ($\eta = 0.79$). (c) TEM image of a GO sheet exhibiting dendritic and polyhedral GNS. (d) TEM image of an individual dendritic-shaped GNS wrapped with a GO sheet prepared by MW exposure to the solution of GO and gold salt maintained at a lower ambient temperature.

MW exposure) suggests that the local dielectric heating from MW induces reduction of gold ions that results in the spontaneous formation of BSGNs. Selected-area electron diffraction

(SAED) patterns of BSGNs (see Supporting Information, Figure S3) indicate monocrystallinity, which also supports the spontaneous formation of these NPs during the short MW exposure. The formation of BSGNs during the MW exposure is proposed to occur in two steps, (1) an instantaneous gold nucleation event, which might attach some gold nuclei on the GO sheets, and (2) the growth of nuclei on GO and in solution. The net rate of BSGN formation during the MW exposure (r_f) can thus be modeled as

$$r_f = r_n + r_g \qquad (1)$$

where r_n and r_g denote the rates for gold nucleation and growth of the nuclei, respectively. The process of nucleation takes place in an instantaneous burst during the MW exposure and hence is expected to have a very high rate constant. On the other hand, the rate of nuclei growth is dependent on the internal solution diffusion of smaller gold nuclei ($k_d \propto T^{1.5}$) and their self-incorporation to form NPs ($k_i \propto \exp(-E_a/RT)$). At the high temperature facilitated by the MW, k_d and k_i assume large values, enabling a high nuclei growth rate that is expected to form regular sharp-edged gold nanostructures, as we observed.[27]

The presence of floating NP-stabilizing templates in solution (facilitated by GO sheets) enabled us to determine key factors which govern the formation of NPs during MW exposure. This was achieved by changing the ambient reaction temperature and observing its effect on the morphology of thus-formed NPs. When the ambient temperature of the reaction mixture was decreased (by placing the solution in an ice bath during microwave exposure), a small incidence of BSGNs were found to exhibit dendritic morphologies (Figures 1c and 3c and Supporting Information, Figure S5). At lower temperature, the resistances offered to the internal diffusion ($k_d^{-1} \propto T^{-1.5}$) and particle self-incorporation ($k_i^{-1} \propto \exp(E_a/RT)$) increased, making the growth of nuclei partly diffusion-limited. A diffusion-limited growth in the presence of molecular anisotropy results in the formation of dendritic structures.[39] The observed dendritic morphologies can be attributed to diffusion-limited hierarchical fusion of smaller gold nuclei, followed by anisotropic preferential growth on the sharp surfaces which exhibit higher chemical potentials [$\mu(R = \text{constant}) > \mu(R = \infty)$, Mullins–Sekereka instability[40]]. Only a small incidence of NPs assumes dendritic shapes as it is difficult to lower the solution temperature homogeneously during MW exposure.

For a prolonged MW exposure duration (~3 min), some dendritic gold nanostructures suspended in solution also get wrapped/encapsulated within the GO sheets. (Figure 3d; also see Supporting Information, Figure S6). The encapsulation of NPs by GO sheets is driven by the covalent interaction forces between their surfaces; however, the complete mechanism needs more studies. Encapsulation of in-situ-formed Ag nanoparticles by GO sheets was reported earlier, where an optimal thickness (0.5 nm) and size (~1.5×10^{-3} μm^2) of the GO sheet was considered essential for the event of GO wrapping.[41] Here, since the NP formation during the short MW exposure precedes their implantation on GO and several GO sheets exhibit large surface areas (>1000 μm^2) with multiple-layer thickness (>1.5 nm), we observe a larger percentage of NP implants on GO sheets as compared to NPs wrapped with GO.

The absence of a chemical reducing agent makes this process fundamentally different from other solution-based GO–metal NP fabrication routes.[27−30] The solution of BSGN-decorated GO sheets was stable for at least 60 days. In addition to the oxy-functional groups, the excellent stabilizing ability of GO sheets can also be ascribed to their micrometer-size surface area, which keeps the nuclei segregated in solution and reduces their coagulation probability.

The dispersion density of BSGNs on GO can be enhanced by increasing the time of interaction between the microwaved gold salt solution and the GO sheets. Figure 3b shows a BSGN–GO sheet that was incubated for ~72 h before immobilizing on the silica substrate. This GO sheet exhibits a higher surface coverage index ($\eta = 0.79$) (see also Supporting Information, Figure S4) than the GO sheet incubated for ~24 h ($\eta = 0.31$). This observation suggests that BSGN implantation on GO is a diffusion-limited process. Thus, by increasing the time of interaction between the microwaved gold salt solution and GO sheets, it is possible to significantly decrease the number of unassembled/unwrapped BSGNs and obtain a GO–BSGN composite dominant solution.

To probe the nature of interaction between the BSGNs and the GO surface, the GO–BSGN composites were analyzed for their Raman spectra. The D band line (1340 cm^{-1}) and G band line (1590 cm^{-1}) observed in the Raman spectrum of the GO sheet were found to be enhanced by ~300% by the presence of BSGNs (Figure 4a). This observed Raman signal enhancement is similar to the SERS effects that we reported earlier for metal nanoparticle composites of GO and suggests a chemical interaction between BSGNs and oxy-functional groups on GO.[19]

Here, we report the catalytic properties of the solution-dispersed GO–BSGN sheets for the GNP-catalyzed reduction of 4-nitroaniline (4-NA) to p-phenylene diamine (p-PDA) in the presence of NaBH$_4$.

$$4\text{-nitroaniline} + NaBH_4 \xrightarrow{\text{GNPs}} p\text{-phenylene diamine}$$
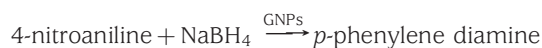
The reaction rate is monitored by successive UV–vis absorbance measurements of the reaction solution (4-NA + NaBH$_4$ → p-PDA) as 4-NA and p-PDA exhibit distinct peaks at 380 and 238 nm, respectively. With the progress of reaction, the light-yellowish-colored 4-NA solution gradually turns colorless with the formation of p-PDA. In the presence of BSGNs–GO, the average reaction time (t_r) was ~8 min (Figure 4b). This reaction with the GO-supported BSGNs as catalysts is ~10-fold faster than that reported in the literature for reduction using gold NPs as catalysts ($t_r = 86$ min) and ~100-fold faster than the reduction using copper NP catalysts ($t_r = 8$−12 h) under identical conditions (see Experimental Section).[42,43]

Motivated by this excellent catalytic ability of BSGNs on GO and the fact that the catalytic rate constant of the GNPs increases with a decrease in the NP size, we synthesized GO-supported smaller GNP seeds (5−20 nm) by an in situ NaBH$_4$ reduction of gold salt (see Experimental Section). These smaller-sized spherical GNPs stabilized on GO are utilized to correlate the presence of a bare surface in the
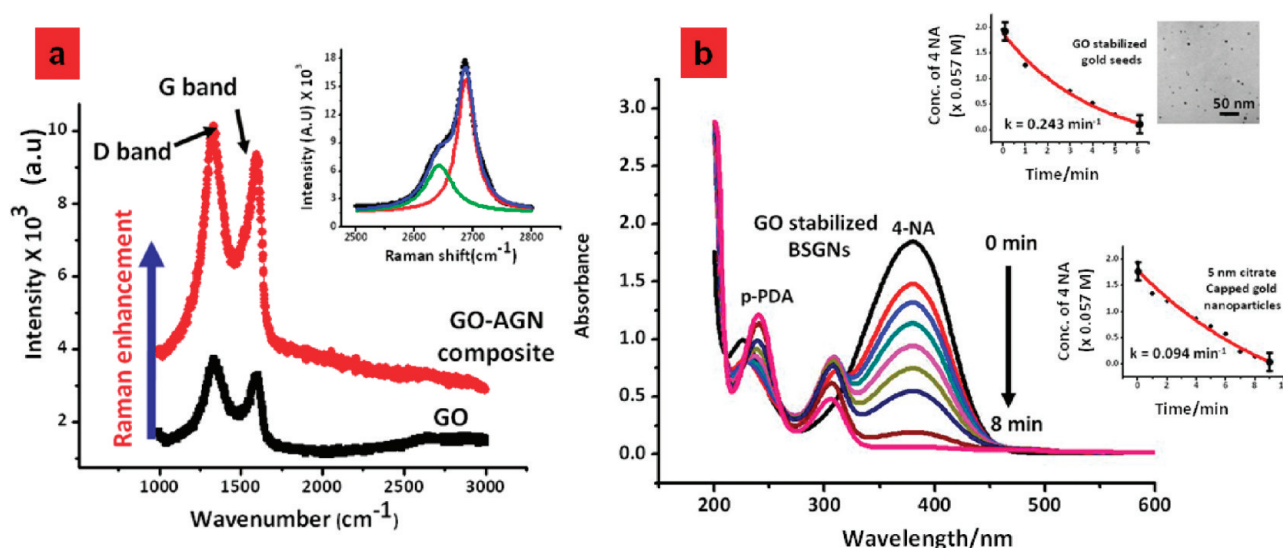
Figure 4. (a) The presence of BSGNs enhances the native Raman spectra of GO sheets by 300%, characteristic for a chemical enhancement, suggesting that the BSGNs chemically attach to the oxy-functional groups on GO. The inset shows the Lorentzian fit to the 2D band of the Raman spectra of GO and GO−BSGN sheets showing the presence of two components, which suggests a characteristic of few-layered graphene. (b) BSGNs stabilized on GO sheets were studied for their catalytic activity for $NaBH_4$-induced reduction of 4-nitroaniline (4-NA). The reaction time can be evaluated by monitoring the successive decrease of the band at 380 nm for 4-NA and the corresponding increase in the band at 238 nm for *p*-phenylene diamine. Complete reduction of 4-NA in the presence of BSGNs stabilized on GO takes ~8 min. The insets show the first-order exponential fits for the reaction catalyzed by GO−gold seeds and 5 nm citrate-capped GNPs. The rate constants are found to be 0.243 and 0.094 min^{-1} respectively.

GO-supported gold seeds with the catalytic efficiency by comparing their catalytic activities with 5 nm citrate-capped gold nanoparticles. It is pertinent to mention that establishing this correlation by utilizing the BSGNs synthesized by the MW method is challenging as they exhibit multiple shapes and hence cannot be directly compared for their catalytic activities with the citrate-stabilized spherical GNPs. The concentration of gold seeds/NPs in both solutions is made equivalent to ~10^{13}/ML. The complete reduction of 4-NA takes ~6 min in the presence of GO−gold seeds and ~8 min in the presence of 5 nm citrate-capped GNPs, with their first-order rate constants calculated to be $k_{GO-gold seeds} = 0.243$ min^{-1} and $k_{5 nm GNPs} = 0.094$ min^{-1}, respectively (Figure 4b insets), suggesting that the gold seeds stabilized on GO have a higher catalytic activity than similar-shaped surfactant-coated gold nanoparticles. Since the activity can be assumed to be directly proportional to the reaction rate constant, the active gold sites due to the naked surface on GO−gold seeds increase by a factor of $I_{obs} = k_{GO-gold seeds}/k_{5 nm GNPs} = 258$%. The theoretical increase in the active gold sites (I_{theo}) on GO−gold seeds due to their naked surface (without including the effect of steric hindrance) can be given by

$$I_{theo} = \frac{f \times A_{gn}}{f \times A_{cp}} \quad (2)$$

where, f is the fraction of catalytically active sites that are available per unit area on the bare surface of a spherical gold nanoparticle, A_{gn} is the bare area on the exposed semisurface of the GO-stabilized gold seed, and A_{cp} denotes the bare area on the citrate-capped GNP. We assume the rear-implanted semisurface of the GO−gold seed to be unavailable for catalytic participation. For a GNP/GO−gold seed with radius

r, $A_{gn} = 2\pi r^2$ and $A_{cp} = 4\pi r^2 \times (1 - \partial)$, where ∂ is the fraction of the GNP surface area covered by the surfactant molecules. For N surfactant molecules adsorbed on a GNP with the projected area of the surfactant molecule = a_s

$$\partial = \frac{N \times a_s}{4\pi r^2} \quad (3)$$

For an equimolar concentration of gold salt and sodium tricitrate, N and a_s can be calculated as follows:

$$N = \frac{N_A \times \rho_{gold} \times \frac{4\pi r^3}{3}}{MW_{gold salt}} \quad (4)$$

$$a_s = \pi r_0^2 \quad (5)$$

Here, a_s is approximated as the projected surface area of the carboxylic oxygen (radius = r_o) through which the citrate molecule binds to the GNP surface. For N_A(Avogadro's constant) = 6.023×10^{23}, $r = 5$ nm, $r_o = 66$ pm, $\rho_{gold} = 19.3$ g/cm³, and $MW_{gold} = 393.8$, N is calculated to be 1.54×10^4, and ∂ is calculated to be 0.671. Substituting N and ∂ in eq 3, I_{theo} is calculated to be ~152%, comparable to the value of $I_{obs} = 258$%. Since the I_{theo} estimation does not consider the effect of steric hindrance from the surfactant molecules in the citrate-capped GNPs, the number of active sites on citrate-capped GNPs is overestimated. Hence, I_{theo} represents a lower bound of the increase in catalytically active sites due to the naked surface on the GO−gold seed. Clearly, the naked gold surface also benefits from the loss of steric hindrance as well.

We envision that the catalytic applications of the GO−BSGN composite will further benefit from the following facts: (1) GNPs catalyze a wide range of reactions with high selectivity,
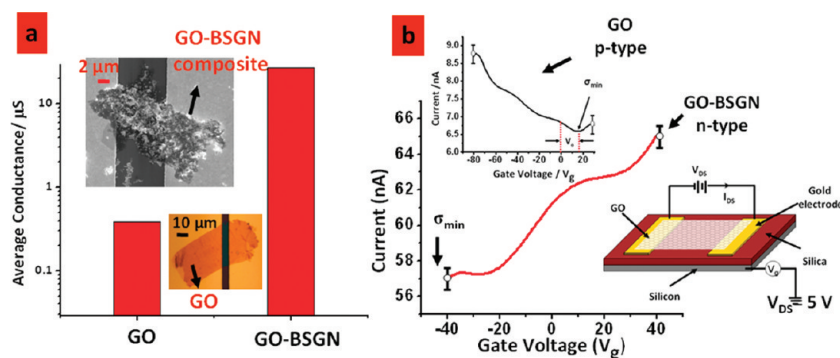
Figure 5. (a) BSGNs enhance the average conductance of GO sheets by an order of magnitude. The top inset shows the FESEM image of the surface-immobilized GO−BSGN composite, and the bottom inset shows the optical image of a GO sheet in between gold electrodes. (b) The effect of BSGNs on the nature of charge carriers in GO is determined by comparing the gating behavior of GO and GO−BSGN at a constant source−drain voltage (V_{DS}) of 5 V. The top inset shows the gating behavior of GO, which exhibits a p-type semiconducting behavior; the Dirac neutrality point is situated at 18 V. In the presence of BSGNs, the Dirac neutrality point shift towards negative voltages, making GO−BSGN an n-type semiconductor. The bottom inset shows the schematic for the gating setup.

the kinetics of which can be significantly improved by substituting the stabilizing-agent-capped GNPs with GO-supported BSGNs; (2) the ability of the graphene platform to store and transfer electrons enhances the access paths available for electron transfer during the course of reaction, making it an ideal support material for the catalytic NPs; (3) (studied here) the GO−BSGN sheets can be suspended in several organic solvents, such as tetrahydrofuran, N-methyl-2-pyrrolidone, N,N-dimethylformamide, and ethylene glycol; (4) the GO−BSGN composite films on metal electrodes (such as Pt) can be used for electrocatalytic applications; and (5) the strong covalent interfacing of GNPs with GO would reduce catalyst poisoning.

For electrical characterization, GO and GO−BSGN composite sheets were immobilized on an amine-silanized silica on an n++ silicon substrate with prepatterned interdigitated gold electrodes. The Figure 5a insets show the FESEM and optical images of GO−BSGN and GO sheets deposited in between gold electrodes. Both devices had multilayered GO and GO−BSGN sheets (> 5), as inferred by the Lorentzian analysis of the 2D band in their Raman spectra that comprises two components, which is characteristic of few-layer graphene (Figure 4a inset). Figure 5a compares the conductance of GO and GO−BSGN averaged over multiple samples. The average conductance of the GO−BSGN device (27.02 μS) was found to be ∼700% higher than that of the GO devices (0.387 μS). This is attributed to the high density of gold islands on the GO surface, which offer a lower resistance to the carrier flow. The GO−BSGN ensemble can be modeled as an assembly of percolating BSGNs configured in parallel to the underlying GO surface, such that

$$R_{GO-BSGN} = \frac{R_{GO} \times R_{BSGN}}{R_{GO} + R_{BSGN}} < R_{GO} \qquad (6)$$

We studied the effect of BSGN interfacing on the nature of majority charge carriers of the GO sheets by conducting gating studies on GO and GO−BSGN samples. Gating was performed at a source−drain voltage, V_{DS} = 5 V, and by measuring the change in conductivity with the gate voltage

applied to the heavily doped silicon backgate (Figure 5b bottom inset) under a 300 nm silica gate oxide. The surface charge density (n_o) induced upon application of a gate voltage (V_g) can be calculated as

$$n_o = \frac{\varepsilon_o \times \varepsilon \times V_g}{d \times e} \qquad (7)$$

where ε_o and ε are the relative permittivity of free space and silica respectively, e is the electron charge, and d is the thickness of the SiO$_2$ layer. GO exhibits a p-type semiconducting behavior, with a positive Dirac neutrality point located at V_g = 18 V (Figure 5b top inset). For the GO−BSGN sheet, the Dirac neutrality point is shifted toward large negative gate voltages, suggesting that the BSGNs inject electrons into the GO surface. The positive Dirac point of V_o = 18 V in the p-type GO suggests that at least 1.328×10^{12} holes cm^{-2} in GO were paired with electrons during BSGN implantation ($V_g = V_o$ = 18 V, ε = 4, ε_o = 8.85 × 10^{-12} F/m, d = 300 nm, and e = 1.6 × 10^{-19} C) to produce n-type GO−BSGN. The electron injection density is expected to be proportional to the GNP size and implantation density. Therefore, by controlling the implantation process, the carrier properties of the GO−BSGN can be tuned, thus opening avenues for fabricating graphene-based p−n junction devices with controllable electronic properties.

Similar to gold, silver nanostructures were also stabilized on GO via the microwave process. Microwaving silver salt (AgNO$_3$) in the presence of GO sheets results in the formation of GO-stabilized spherical and tadpole-shaped Ag NPs (Supporting Information, Figures S9 and S10), suggesting the excellent adaptability of the MW method, making it a highly prospective tool for interfacing GO with diverse metal NPs

In summary, this work presents a potential solution to a major challenge in liquid-phase catalysis by enabling the synthesis of stable liquid dispersions of uncapped metal nanoparticles with enhanced density of accessible catalytic sites. This is achieved by the implantation of MW-nucleated NPs on the GO acting as a stabilization agent for GNPs. Remarkably, these naked BSGNs possess 258% higher density of

catalytically active atomic sites, which enhance the catalytic reduction of *p*-nitroaniline 10−100 fold. Further, the BSGNs enhance the Raman signal of GO 3 fold and inject 1.328×10^{12} electrons into the p-type GO to make it n-type, thus enabling the manipulation of its carrier density. We envision that the results presented here will evolve the fields of liquid-phase catalysis, graphene nanotechnology, and electronics, and this highly versatile process will potentially produce next-generation supported catalysts, graphene hybrids, optoelectronic devices, sensors, Raman multipliers, and molecular electronics.

EXPERIMENTAL SECTION

Preparation of Graphene Oxide (GO). Five grams of Mesh 7 graphite flakes was mixed with 33 mL of 68% nitric acid plus 200 mL of 96% sulfuric acid and stirred continuously for 40 min in an ice bath; 30 g of potassium permanganate was then added into the solution while the temperature was slowly increased to 40 °C and kept at 400 °C for 30 min. Subsequently, the excess potassium permanganate was removed by treatment with 10% hydrogen peroxide. Finally, the GO sheets were obtained by centrifuging this solution at 15000 rpm for 30 min followed by repeated washing with DI water. The sample was then dialyzed (MWCO 2000D) for 24 h and then subsequently stored as a suspension in DI water at room temperature.

Preparation of Bare-Surfaced Gold Nanostructures (BSGNs) Templated on GO Sheets. The GO−BSGN nanocomposite was synthesized by MW exposure (1.05 kW, 2450 MHz) on an aqueous solution of GO (100 μL, 20 mM carboxylic acid quantified by titration) and gold salt, $HAuCl_4 \cdot 3H_2O$ (10 mL, 0.275 mM) for a time interval between 60 and 300 s with intermittent cooling after every 10 s. The mixture was allowed to stand for ~24 h, which resulted in the formation of BSGNs with triangular, hexagonal, and dendritic morphologies, which either assemble on or get wrapped with the GO sheets, depending on the MW exposure time.

TEM and SAED. TEM images and SAED patterns were obtained with a Philips CM 100 transmission electron microscope operated at 100 kV by depositing the GO−AGN hybrids from solution onto a 300 mesh size copper grid.

FESEM. FESEM Images were obtained with a Leo field emission scanning electron microscope operated at 10−15 kV.

Electrical Conductivity and Gating Measurements. All electrical measurements were taken at room temperature under a steady nitrogen environment using a Keithley 2612 dual-channel system source meter connected to a computer via a GPIB/IEEE-488 interface card.

Raman Spectroscopic Measurements. The Raman spectra of GO and GO−BSGN sheets were determined by using a LabRAM ARAMIS Raman spectrometer located at the University of Kansas, Bioengineering Research Center, Lawrence, KS. The instrument was manufactured by HORIBA Jobin Yvon (Edison, New Jersey), and a HeNe laser ($l = 633$ nm, a laser power of 17 mW) was used as one of the excitation sources for the samples. The instrument conditions were a 200 μm confocal hole, 150 μm wide entrance slit, 600 gr/mm grating, and 100× objective Olympus lens. Data processing was performed using LabSPEC 5 (HORIBA Jobin Yvon). The samples were mounted in a computer-controlled, high-precision x−y stage.

Catalytic Measurements. For the catalytic reaction, 600 μL of a 10^{-3} M 4-NA solution was mixed with 4 mL of DI water followed by an addition of 600 μL of 0.1 M $NaBH_4$; 600 μL of the as prepared solution of GO−BSGN was added to study the catalytic activity of these nanostructures. Assuming a complete conversion of gold salt into NPs, the average concentration of BSGNs was calculated to be ~10^{13}/ml. For catalytic activity comparison experiments, citrate-capped NPs with the same concentration were used.

AUTHOR INFORMATION

Corresponding Author:

*To whom correspondence should be addressed. E-mail: vberry@ksu.edu.

REFERENCES

(1) Katsnelson, M. I.; Novoselov, K. S.; Geim, A. K. Chiral Tunnelling and the Klein Paradox in Graphene. *Nat. Phys.* **2006**, *2*, 620–625.

(2) Novoselov, K. S.; Jiang, Z.; Zhang, Y.; Morozov, S. V.; Stormer, H. L.; Zeitler, U.; Maan, J. C.; Boebinger, G. S.; Kim, P.; Geim, A. K. Room-Temperature Quantum Hall Effect in Graphene. *Science* **2007**, *315*, 1379.

(3) Wang, F.; Zhang, Y.; Tian, C.; Girit, C.; Zettl, A.; Crommie, M.; Shen, Y. R. Gate-Variable Optical Transitions in Graphene. *Science* **2008**, *320*, 206.

(4) Blake, P.; Brimicombe, P. D.; Nair, R. R.; Booth, T. J.; Jiang, D.; Schedin, F.; Ponomarenko, L. A.; Morozov, S. V.; Gleeson, H. F.; Hill, E. W.; et al. Graphene-Based Liquid Crystal Device. *Nano Lett.* **2008**, *8*, 1704–1708.

(5) Wright, A. R.; Xu, X. G.; Cao, J. C.; Zhang, C. Strong Nonlinear Optical Response of Graphene in the Terahertz Regime. *Appl. Phys. Lett.* **2009**, *95*, 072101.

(6) Xu, X.; Gabor, N. M.; Alden, J. S.; van der Zande, A. M.; McEuen, P. L. Photo-Thermoelectric Effect at a Graphene Interface Junction. *Nano Lett.* **2010**, *10*, 562–566.

(7) Lee, C.; Wei, X. D.; Kysar, J. W.; Hone, J. Measurement of the Elastic Properties and Intrinsic Strength of Monolayer Graphene. *Science* **2008**, *321*, 385–388.

(8) Mohanty, N.; Berry, V. Graphene-Based Single-Bacterium Resolution Biodevice and DNA Transistor: Interfacing Graphene Derivatives with Nanoscale and Microscale Biocomponents. *Nano Lett.* **2008,** *8,* 4469–4476.

(9) Lu, C. H.; Yang, H. H.; Zhu, C. L.; Chen, X.; Chen, G. N. A Graphene Platform for Sensing Biomolecules. *Angew. Chem., Int. Ed.* **2009,** *48,* 4785–4787.

(10) Liu, Z.; Robinson, J. T.; Sun, X.; Dai, H. PEGylated Nanographene Oxide for Delivery of Water-Insoluble Cancer Drugs. *J. Am. Chem. Soc.* **2008,** *130,* 10876–10877.

(11) Sundaram, R. S.; Gomez-Navarro, C.; Balasubramanian, K.; Burghard, M.; Kern, K. Electrochemical Modification of Graphene. *Adv. Mater.* **2008,** *20,* 3050–3053.

(12) Wu, Z. S.; Pei, S.; Ren, W.; Tang, D.; Gao, L.; Liu, B.; Li, F.; Liu, C.; Cheng, H. M. Field Emission of Single-Layer Graphene Films Prepared by Electrophoretic Deposition. *Adv. Mater.* **2009,** *21,* 1756–1760.

(13) Bunch, J. S.; Verbridge, S. S.; Alden, J. S.; van der Zande, A. M.; Parpia, J. M.; Craighead, H. G.; McEuen, P. L. Impermeable Atomic Membranes from Graphene Sheets. *Nano Lett.* **2008,** *8,* 2458–2462.

(14) Ramanathan, T.; Abdala, A. A.; Stankovich, S.; Dikin, D. A.; Herrera-Alonso, M.; Piner, R. D.; Adamson, D. H.; Schniepp, H. C.; Chen, X.; Ruoff, R. S.; et al. Functionalized Graphene Sheets for Polymer Nanocomposites. *Nat. Nanotechnol.* **2008,** *3,* 327–331.

(15) Stankovich, S.; Dikin, D. A.; Dommett, G. H. B.; Kohlhaas, K. M.; Zimney, E. J.; Stach, E. A.; Piner, R. D.; Nguyen, S. T.; Ruoff, R. S. Graphene-Based Composite Materials. *Nature* **2006,** *442,* 282–286.

(16) Li, J.; Guo, S.; Zhai, Y.; Wang, E. Nafion-Graphene Nanocomposite Film As Enhanced Sensing Platform for Ultrasensitive Determination of Cadmium. *Electrochem. Commun.* **2009,** *11,* 1085–1088.

(17) Fowler, J. D.; Allen, M. J.; Tung, V. C.; Yang, Y.; Kaner, R. B.; Weiller, B. H. Practical Chemical Sensors from Chemically Derived Graphene. *ACS Nano* **2009,** *3,* 301–306.

(18) Williams, G.; Seger, B.; Kamat, P. V. TiO2-Graphene Nanocomposites. UV-Assisted Photocatalytic Reduction of Graphene Oxide. *ACS Nano* **2008,** *2,* 1487–1491.

(19) Jasuja, K.; Berry, V. Implantation and Growth of Dendritic Gold Nanostructures on Graphene Derivatives: Electrical Property Tailoring and Raman Enhancement. *ACS Nano* **2009,** *3,* 2358–2366.

(20) Si, Y.; Samulski, E. T. Exfoliated Graphene Separated by Platinum Nanoparticles. *Chem. Mater.* **2008,** *20,* 6792–6797.

(21) Wang, X.; Tabakman, S. M.; Dai, H. Atomic Layer Deposition of Metal Oxides on Pristine and Functionalized Graphene. *J. Am. Chem. Soc.* **2008,** *130,* 8152–8153.

(22) Comotti, M.; la Pina, C.; Matarrese, R.; Rossi, M. The Catalytic Activity of "Naked" Gold Particles. *Angew. Chem., Int. Ed.* **2004,** *43,* 5812–5815.

(23) Chen, M. S.; Goodman, D. W. The Structure of Catalytically Active Gold on Titania. *Science* **2004,** *306,* 252.

(24) Majetich, G.; Hicks, R. Applications Of Microwave-Accelerated Organic Synthesis: Theory and Applications of Microwave Radiation. *Radiat. Phys. Chem.* **1995,** *45,* 567–579.

(25) Landry, C. C.; Barron, A. R. Synthesis of Polycrystalline Chalcopyrite Semiconductors by Microwave Irradiation. *Science* **1993,** *260,* 1653–1655.

(26) Lee, Y. T.; Choi, S. Y.; Lee, S. I.; Chung, Y. K.; Kang, T. J. Microwave-Assisted Synthesis of (6-Arene) Tricarbonylchromium Complexes. *Tetrahedron Lett.* **2006,** *47,* 6569–6572.

(27) Tsuji, M.; Hashimoto, M.; Nishizawa, Y.; Tsuji, T. Synthesis of Gold Nanorods And Nanowires By a Microwave-Polyol Method. *Mater. Lett.* **2004,** *58,* 2326–2330.

(28) Tu, W.; Liu, H. Rapid Synthesis of Nanoscale Colloidal Metal Clusters by Microwave Irradiation. *J. Mater. Chem.* **2000,** *10,* 2207–2211.

(29) Liu, F. K.; Ker, C. J.; Chang, Y. C.; Ko, F. H.; Chu, T. C.; Dai, B. T. Microwave Heating for the Preparation of Nanometer Gold Particles. *Jpn. J. Appl. Phys.* **2003,** *42,* 4152–4158.

(30) Pastoriza-Santos, I.; Liz-Marzan, L. M. Formation of PVP-Protected Metal Nanoparticles in DMF. *Langmuir* **2002,** *18,* 2888–2894.

(31) Fan, C.; Li, W.; Zhao, S.; Chen, J.; Li, X. Efficient One Pot Synthesis of Chitosan-Induced Gold Nanoparticles by Microwave Irradiation. *Mater. Lett.* **2008,** *62,* 3518–3520.

(32) Tsuji, M.; Matsumoto, K.; Tsuji, T.; Kawazumi, H. Rapid Synthesis of Gold Nanostructures by a Microwave−Polyol Method with the Assistance of C_nTAB (n = 10, 12, 14, 16) or $C_{16}PC$. *Mater. Lett.* **2005,** *59,* 3856–3860.

(33) Wang, J.; Wang, Z. Rapid Synthesis of Hexagon-Shaped Gold Nanoplates by Microwave Assistant Method. *Mater. Lett.* **2007,** *61,* 4149–4151.

(34) Dallinger, D.; Kappe, C. O. Microwave-Assisted Synthesis in Water as Solvent. *Chem. Rev* **2007,** *107,* 2563–2591.

(35) Bi, Y.; Lu, G. Morphological Controlled Synthesis and Catalytic Activities of Gold Nanocrystals. *Mater. Lett.* **2008,** *17−18,* 2696–2699.

(36) Chen, W.; Yan, L.; Bangal, P. R. Preparation of Graphene by the Rapid and Mild Thermal Reduction of Graphene Oxide Induced by Microwaves. *Carbon* **2010,** *48,* 1146–1152.

(37) Murray, C. B.; Kagan, C. R.; Bawendi, M. G. Synthesis and Characterization of Monodisperse Nanocrystals and Close-Packed Nanocrystal Assemblies. *Annu. Rev. Mater. Sci.* **2000,** *30,* 545–610.

(38) Gao, W.; Alemany, L. B.; Ci, L.; Ajayan, P. M. New Insights into the Structure and Reduction of Graphite Oxide. *Nat. Chem.* **2009,** *1,* 403–408.

(39) Nittman, J.; Stanley, H. E. Tip Splitting Without Interfacial Tension and Dendritic Growth Patterns Arising from Molecular Anisotropy. *Nature* **1986,** *321,* 663–668.

(40) Langer, J. S. Instabilities and Pattern Formation in Crystal Growth. *Rev. Mod. Phys.* **1980,** *52,* 1–28.

(41) Cassagneau, T.; Fendler, J. H. Preparation and Layer-By-Layer Self-Assembly of Silver Nanoparticles Capped by Graphite Oxide Nanosheets. *J. Phys. Chem. B* **1999,** *103,* 1789–1793.

(42) Saha, A.; Ranu, B. Highly Chemoselective Reduction of Aromatic Nitro Compounds by Copper Nanoparticles/Ammonium Formate. *J. Phys. Chem.* **2008,** *73,* 6867–6870.

(43) Kundu, S.; lau, S.; Liang, H. Shape-Controlled Catalysis by Cetyltrimethylammonium Bromide Terminated Gold Nanospheres, Nanorods, and Nanoprisms. *J. Phys. Chem. C* **2009,** *113,* 5150–5156.